Facile cascade-anchored synthesis of ultrahigh metal loading single-atom for significantly improved Fenton-like catalysis

Shuaishuai Li, Wei Wang *, Huizhong Wu, Xuechun Wang, shihu Ding, Jingyang Liu, Xiuwu Zhang, Jiangli Sun, Chunhong Fu, Minghua Zhou *

MOE Key Laboratory of Pollution Processes and Environmental Criteria, Tianjin Key Laboratory of Environmental Technology for Complex Trans-Media Pollution, Tianjin Advanced Water Treatment Technology International Joint Research Center, College of Environmental Science and Engineering, Nankai University, Tianjin 300350, China

Carbon Neutrality Interdisciplinary Science Centre, College of Environmental Science and Engineering, Nankai University, Tianjin 300350, China

* Corresponding author. Tel/Fax: +86 022 23501117. E-mail address: zhoumh@nankai.edu.cn (M. Zhou), nkwangwei@126.com

This file includes:

1. Supplementary Notes 1-4

Note 1. Chemicals and Materials

Note 2. Characterization methods

Note 3. Electrochemical measurements

Note 4. Quantum chemical calculations

2. Supplementary Figures 1-29

Fig. 1 | HRTEM images of Fe-SAC-41.31.

Fig. 2 | Raman spectra of as prepared catalysts with different Fe loading.

Fig. 3 | TEM images of Fe-SAC precursor obtained by the a, conventional solvent evaporation method; b, the cascade anchoring strategy.

Fig. 4 | High-resolution XPS spectrum of Fe 2p.

Fig. 5 | High-resolution XPS spectrum of N 1s.

Fig. 6 | The binding energies of the possible CN coordination modes.

Fig. 7 | The structure model of Fe-SAC-5.16.

Fig. 8 | The structure model of Fe-SAC-15.82.

Fig. 9 | The structure model of Fe-SAC-24.62.

Fig. 10 | The structure model of Fe-SAC-41.31.

Fig. 11 | Projected density of state (pDOS) of Fe 3d, N 2p, and C 2p orbital.

Fig. 12 | Top and side views of differential charge density of Fe–SAC-x models.

Fig. 13 | XRD patterns of as-prepared Mn-SAC, La-SAC and Ag-SAC.

Fig. 14 | HAADF-STEM images of a, Mn-SAC; b, La-SAC and c, Ag-SAC.

Fig. 15 | Degradation effect of PMS on SMX.

Fig. 16 | The degradation kinetics of SMX in Fe-SAC-x/PMS system.

Fig. 17 | Iron dissolution of Fe-SAC-x during degradation.

Fig. 18 | a, SMX degradation performance. b, SMX degradation kinetics in the Fe-SAC-41.31/PMS and Fe-SAC-T/PMS system, respectively. Experimental conditions: $[SMX]_0$ = 10 mg L^{-1}, $[PMS]_0$ = 2 mM, pH = 7, catalyst: 0.1g

Fig. 19 | Degradation performance of SMX at different initial concentrations in the a, Fe-SAC-41.31/PMS system b, Fe-SAC-T/PMS system, respectively. Experimental conditions: $[PMS]_0$ = 2 mM, pH = 7, catalyst: 0.1g L^{-1}.

Fig. 20 | Effect of ionic strength on SMX removal in Fe-SAC-41.31/PMS system.

Fig. 21 | Open-circuit potential change of Fe-SAC-41.31 with the addition of SMX.

Fig. 22 | EPR spectra of $^{\bullet}OH$ or $SO_4^{\bullet-}$ in the Fe-SAC-41.31/PMS system.

Fig. 23 | Degradation performance of SMX with continuous injection of N_2 into the Fe-SAC-41.31/PMS system at a rate of 40 mL min^{-1}.

Fig. 24 | EPR spectra of $O_2^{\bullet-}$ in the Fe-SAC-41.31/PMS system.

Fig. 25 | Concentration changes of PMSO and $PMSO_2$ over reaction time. Reaction conditions: $[PMSO]_0$ = 10 mg L^{-1}, [PMS] = 2.0 mM.

Fig. 26 | SMX degradation pathways in the Fe-SAC-41.31/PMS system.

Fig. 27 | Two possible oxygen adsorption configurations of Fe-C2N2 for PMS.

Fig. 28 | a, b, TEM image of Fe-SAC-41.31 before and after the catalytic reaction.

Fig. 29 | a, Design principle of continuous flow device; b, Physical diagram of continuous flow device.

3. Supplementary Tables 1-13

Table 1 | Fe content in varying samples.

Table 2 | BET surface area, pore diameter and mesoporous pore volume of as-prepared catalysts.

Table 3 | EXAFS fitting parameters for various Fe-SAC-x samples.

Table 4 | Element contents and Fe density derived from XPS results.

Table 5 | Catalytic oxidation performances of various catalysts for pollutants.

Table 6 | Intermediates detected by LC-MS in the Fe-SAC-41.31/PMS system.

Table 7 | The adsorption energy and bond length of Fe-O, O-O and O-H in the possible two adsorption configurations.

Table 8 | The Gibbs free-energy (△E) for every step in the two possible pathways of Fe-SAC-41.31 system.

Table 9 | The Gibbs free-energy (△E) for every step in the possible pathway of different catalysts.

Table 10 | The quality parameters of the wastewater.

Table 11 | The quality parameters of the coal reverse osmosis water.

Table 12 | 3DEEM response and their associated characteristics.

Table 13 | The HPLC analysis conditions for different substrates.

4. Supplementary References

1. Supplementary Notes

Chemicals and Materials

Iron nitrate nonahydrate ($Fe(NO_3)_3$ $9H_2O$) and melamine ($C_3H_6N_6$, 99%) were bought from Macklin Ltd. (Shanghai, China). Sodium sulfate (Na_2SO_4), potassium peroxymonosulfate (PMS, $KHSO_5$•$0.5KHSO_4$•$0.5K_2SO_4$), sodium bicarbonate ($NaHCO_3$), sodium dihydrogen phosphate (NaH_2PO_4), sulfuric acid (H_2SO_4), sodium hydroxide (NaOH), potassium thiocyanate (KSCN), 5,5-dimethyl-1-pyrroline N-oxide (DMPO, 97%), methyl phenyl sulfoxide (PMSO) and Furfuryl alcohol (FFA) were purchased from Aladdin Ltd. (Shanghai, China). Methanol (MeOH, 99.9%) was purchased from Tianjin Kemiou Chemical Reagent Co., Ltd (Tianjin, China). Tertbutyl alcohol (TBA, > 99.5%), Nafion solution (5 wt.%) and oxalic acid (OA) were purchased from Sinopharm Group Chemical Reagent Co., Ltd. (Shanghai, China). 2,2,6,6-Tetramethylpiperidine (TEMP) was bought from Tianjin Sinos Opto Technology Co., Ltd (Tianjin, China). The studied model pollutants, bisphenol A (BPA), phenol (BP), Rhodamine B (RhB), tetracycline (TC), methyl orange (MO) and sulfamethoxazole (SMX) were purchased from Aladdin Ltd. (Shanghai, China). All organic solvents were HPLC grade.

Characterization methods

XAS measurements were carried out in transmission mode using a commercial laboratory device (easyXAFS300, easy XAFS LLC, Renton, WA). This instrument is based on Rowland circle geometries and is equipped with spherically bent crystal analyzers (SBCAs) and a silicon drift detector (AXAS-M1, KETEK GmbH, Munich, Germany). The morphologies of catalysts were observed by the transmission electron microscopy (TEM, JEM-2800). Aberration-corrected high-angle annular dark-field scanning transmission electron microscopy (AC-HAADF-STEM) images were recorded on a high resolution transmission electron microscope (JEM-ARM200F) with a field-emission gun at 200 kV. X-ray photoelectron spectroscopy (XPS, Thermo Scientifc ESCALAB 250Xi) was utilized to analyze the bonding state of elements on the catalyst surface. Fourier transformed infrared spectroscopy (FTIR) was conducted by Thermo Scientific Nicolet IS50 FTIR (Thermo Fisher, USA). In-situ FTIR was carried out using an external reflection configuration and the Ge crystal was used as prism. Raman analysis was carried out using a confocal microscopic Raman spectrometer (LabRam HR, Horiba, France). X-ray diffraction (XRD) patterns of catalysts were characterized by a Philips-12045 B/3 diffractometer. BET specific surface areas and pore distribution of the catalysts were measured through a Micromeritics ASAP 2460 instrument. The atomic ratios of Fe in the samples were analyzed using an inductively coupled plasma atomic emission spectrometer (ICP- AES) (IRIS Intrepid II XSP) to reveal the catalyst composition. Electron paramagnetic resonance (EPR) was used to analyze the reactive species by a Bruker EMX Nano (Germany).

Electrochemical measurements

The electrochemical performance was tested by a CHI 760E potentiostat (CH Instruments, Chenhua, Shanghai, China). The catalyst was coated on a glassy carbon electrode as a working electrode (5 mg of catalyst, 50 μL of Nafion and 1 mL of ethanol were mixed by ultrasonication, and 10 μL of the mixture was dropped onto the glassy carbon electrode to dry naturally, the catalyst loading was 0.25 mg cm^{-2}), a platinum sheet was used as the counter electrode, and Ag/AgCl electrode was used as the reference electrode. The electrode potential was converted to a reversible hydrogen electrode (RHE) reference scale using $E_{RHE}=E_{Ag/AgCl}+0.197+0.0592(pH)$. The linear sweep voltammetry (LSV) curve was obtained at the scanning rate of 10 mV s^{-1} in the electrolyte of Na_2SO_4 (50 mM, pH 7). Chronopotentiometry and chronoamperometry analyses were performed to obtain the surface oxidation potential and current response in the reaction system. PMS and SMX samples were added into the electrolyte at stated intervals, with final concentrations of 2 mM and 10 mg L^{-1}, respectively.

Quantum chemical calculations

All spin-polarized density-functional theory (DFT) was calculated through projective enhanced wave method in the Vienna ab initio simulation package (VASP) based on the plane wave base set [1,2]. Generalized gradient approximation (GGA) and PBE parameterization were used to deal with the exchange correlation potential [3]. Grimme's DFT-D3 model was applied for Van der Waals correction (6). To avoid interaction between adjacent images, a vacuum area of about 18 Å was used. The energy cutoff was set at 450 eV. The Brillouin-zone integrals were sampled using a Γ-centered Monkhorst-Pack lattice (2 × 2 × 1). The structure was completely relaxed until the maximum force on each atom was less than 0.02 eV/Å, with an energy convergence criterion of 10^{-5} eV. The free energies (G) of different intermediates are defined as $G = E_i - E_{reactant}$ (E_i is the energy of intermediates and $E_{reactant}$ is the total energy of reactants) and finally obtained by $G = E_{total} + E_{ZPE} - TS$, where E_{total}, E_{ZPE}, and TS are the ground-state energy, zero-point energies, and entropy terms, respectively, with the latter two taking vibration frequencies from DFT.

2. Supplementary Figures 1-29

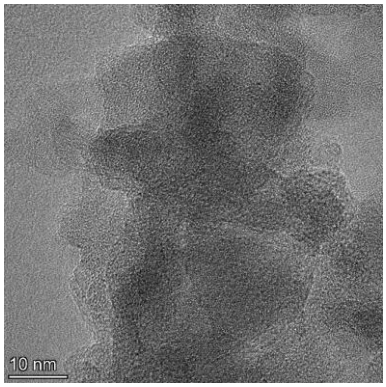

Supplementary Fig. 1 | HRTEM images of Fe-SAC-41.31.

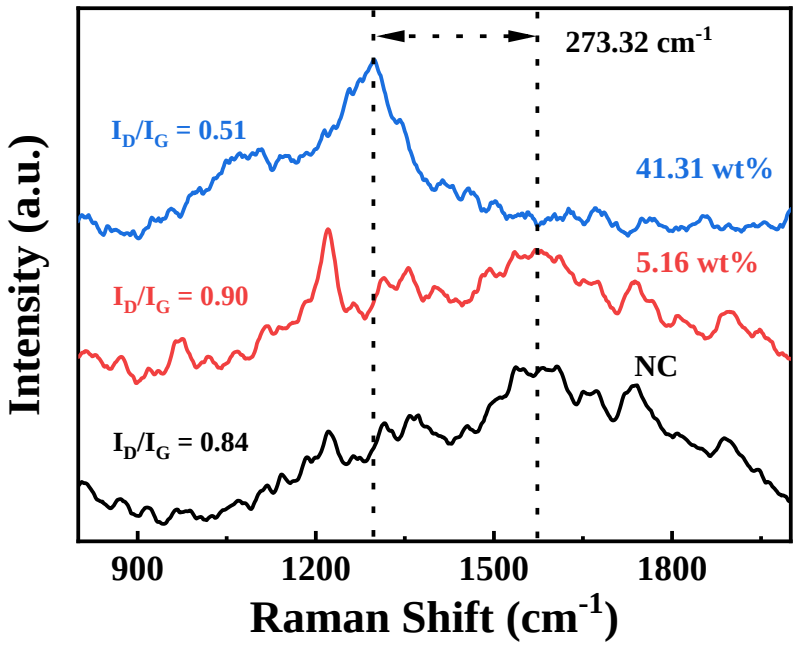

Supplementary Fig. 2 | Raman spectra of as prepared catalysts with different Fe loading.

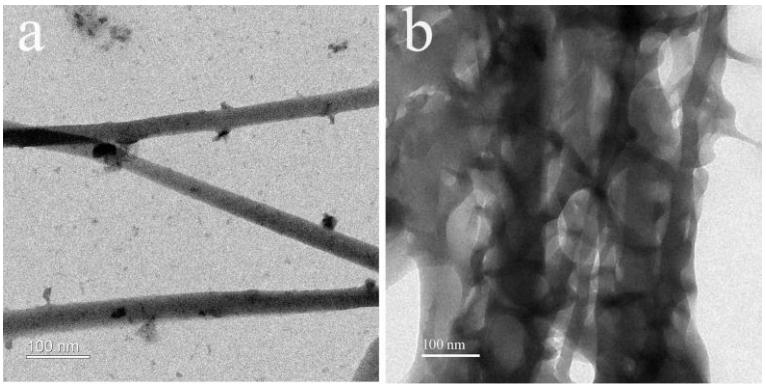

Supplementary Fig. 3 | TEM images of Fe-SAC precursor obtained by the **a**, conventional solvent evaporation method; **b,** the cascade anchoring strategy.

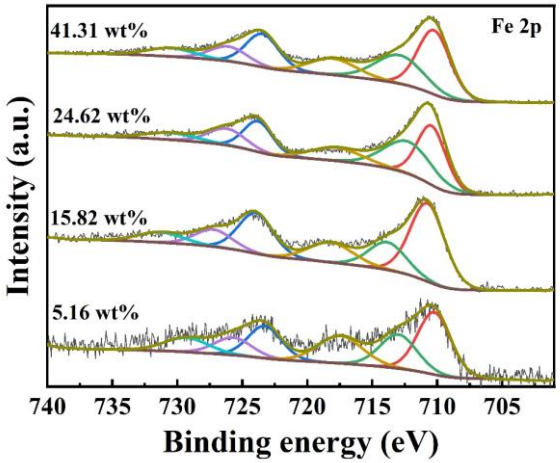

Supplementary Fig. 4 | High-resolution XPS spectrum of Fe 2p.

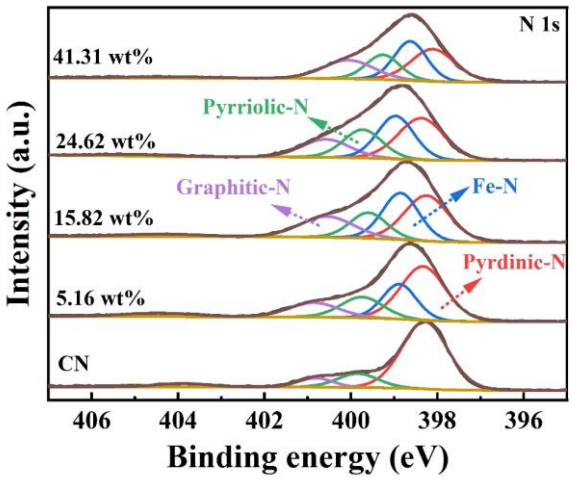

Supplementary Fig. 5 | High-resolution XPS spectrum of N 1s.

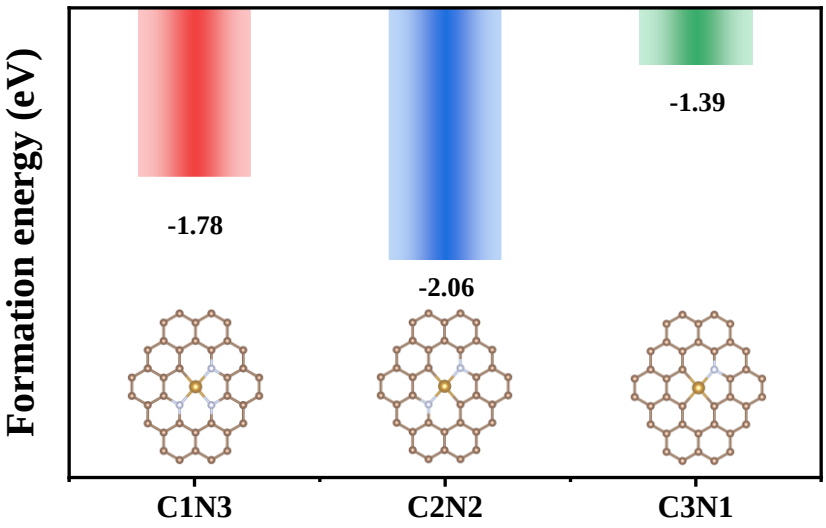

Supplementary Fig. 6 | The binding energies of the possible CN coordination modes.

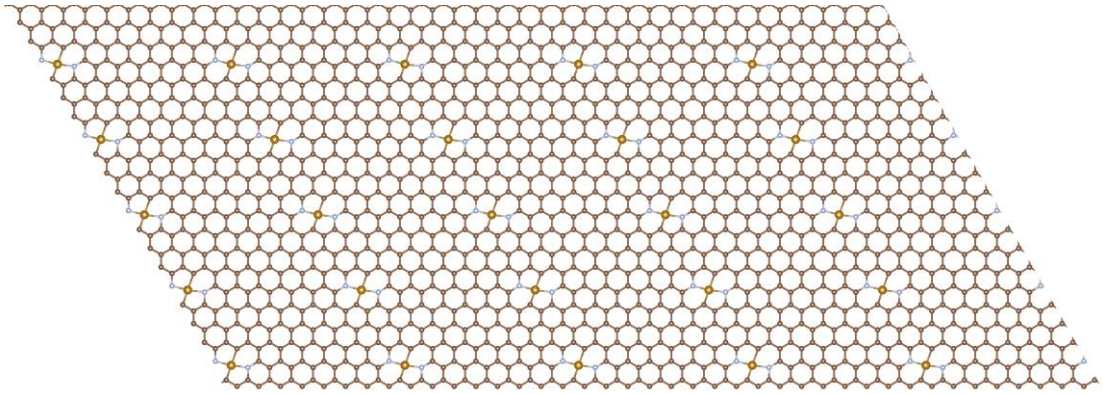

Supplementary Fig. 7 | The structure model of Fe-SAC-5.16.

Sample: Fe-SAC-5.16

Number of atoms: 25 Fe, 50 N, 1561 C

Theoretical Fe loading: $Fe(wt\%)=\frac{25\times56}{25\times56+50\times14+1561\times12}=6.72wt\%$

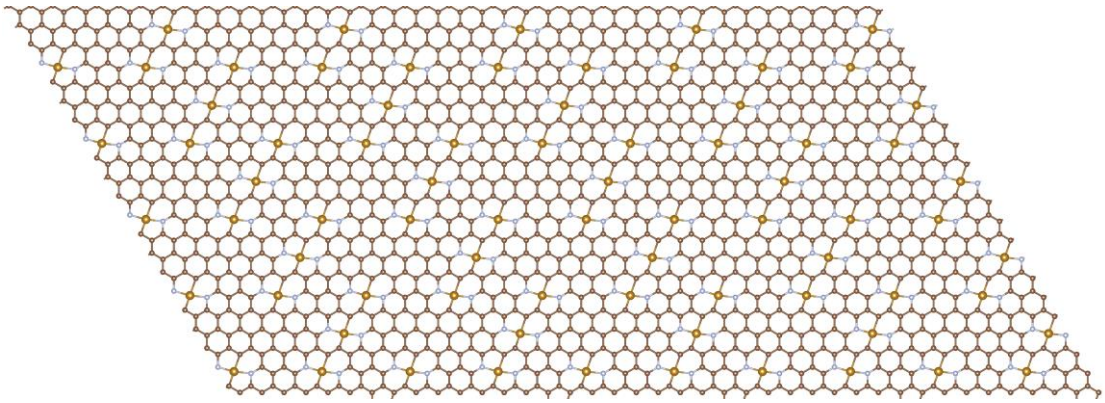

Supplementary Fig. 8 | The structure model of Fe-SAC-15.82.

Sample: Fe-SAC-15.82

Number of atoms: 75 Fe, 150 N, 1361 C

Theoretical Fe loading: $Fe(wt\%)=\frac{75\times56}{75\times56+75\times14+1361\times12}=19.46wt\%$

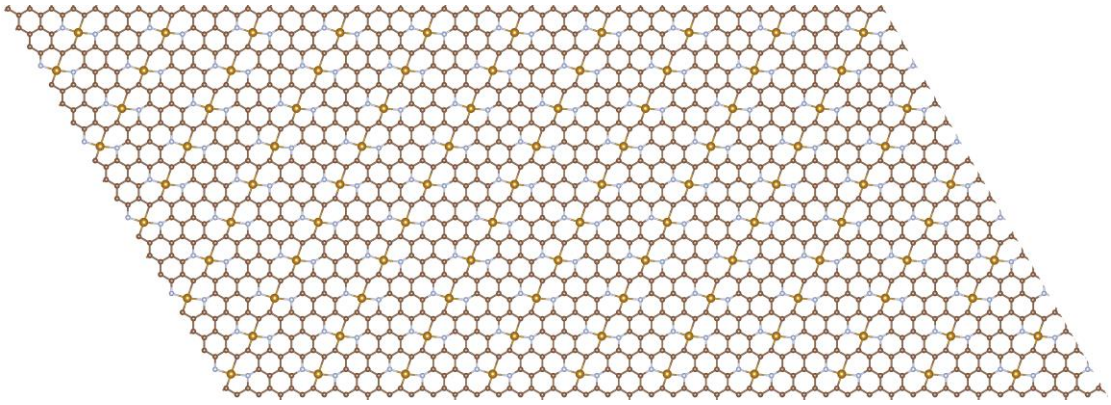

Supplementary Fig. 9 | The structure model of Fe-SAC-24.62.

Sample: Fe-SAC-24.62

Number of atoms: 100 Fe, 200 N, 1261 C

Theoretical Fe loading: $Fe(wt\%)=\frac{100\times56}{100\times56++200\times14+1261\times12}=24.79wt\%$

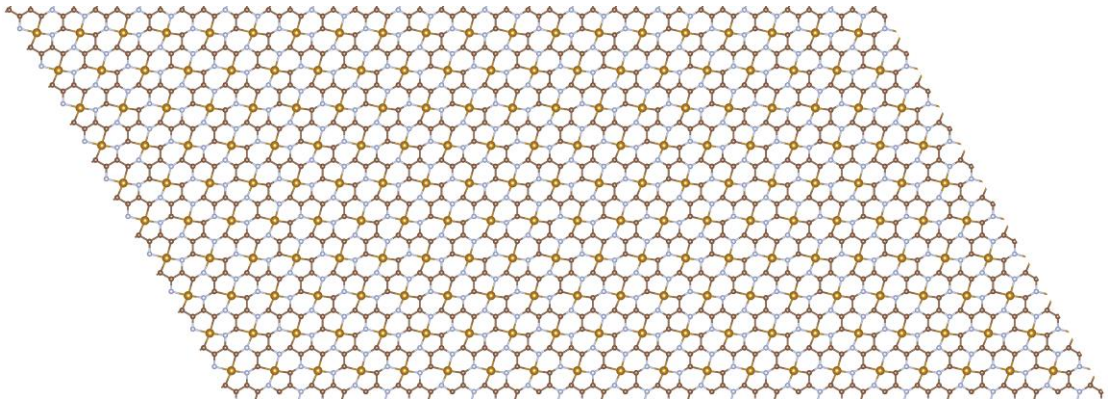

Supplementary Fig. 10 | The structure model of Fe-SAC-41.31.

Sample: Fe-SAC-41.31

Number of atoms: 200 Fe, 400 N, 861 C

Theoretical Fe loading: $Fe(wt\%)=\frac{200\times56}{200\times56++400\times14+861\times12}=41.28wt\%$

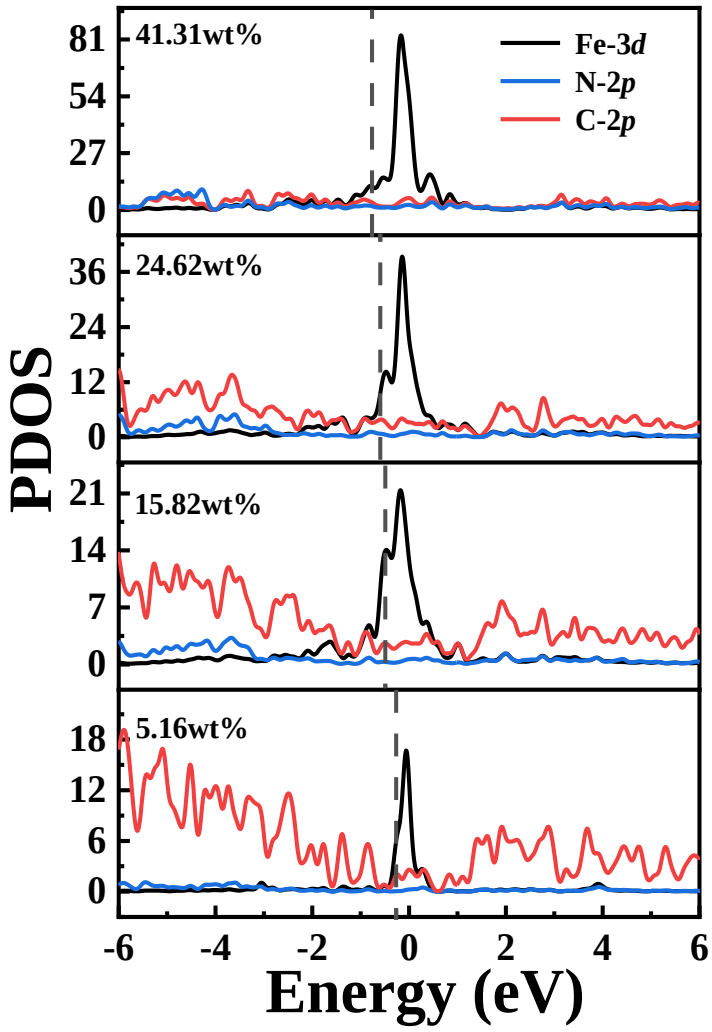

Supplementary Fig. 11 | Projected density of state (pDOS) of Fe 3d, N 2p, and C 2p orbital.

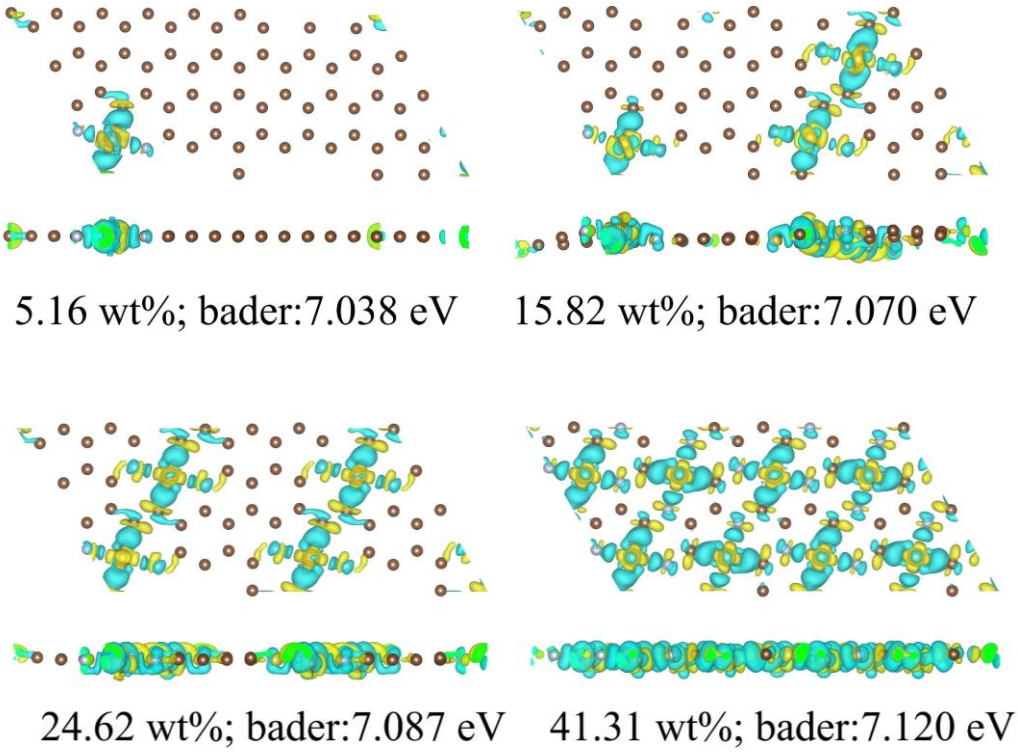

Supplementary Fig. 12 | Top and side views of differential charge density of Fe–SAC-x models.

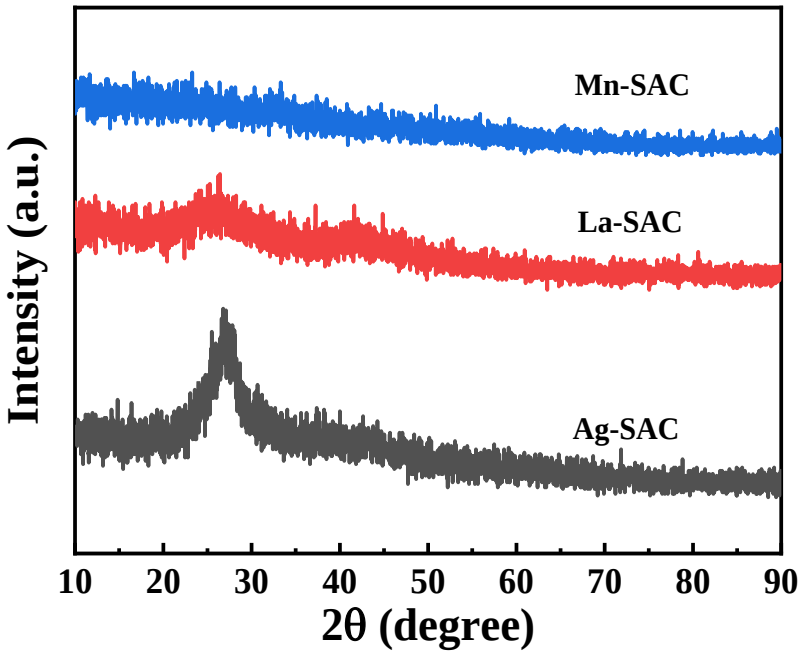

Supplementary Fig. 13 | XRD patterns of as-prepared Mn-SAC, La-SAC and Ag-SAC.

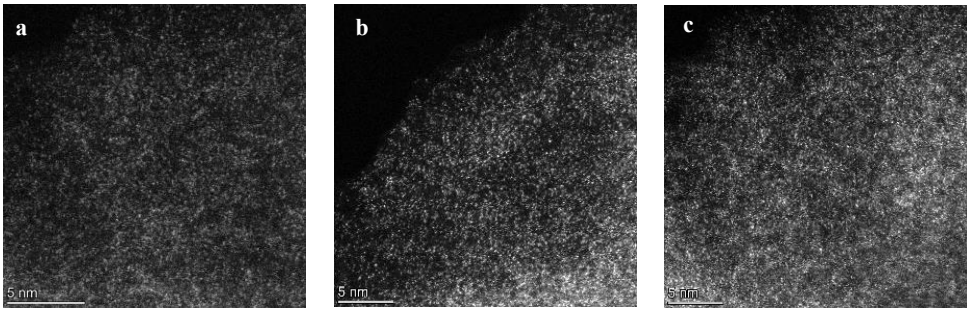

Supplementary Fig. 14 | HAADF-STEM images of **a,** Mn-SAC; **b,** La-SAC and **c,** Ag-SAC.

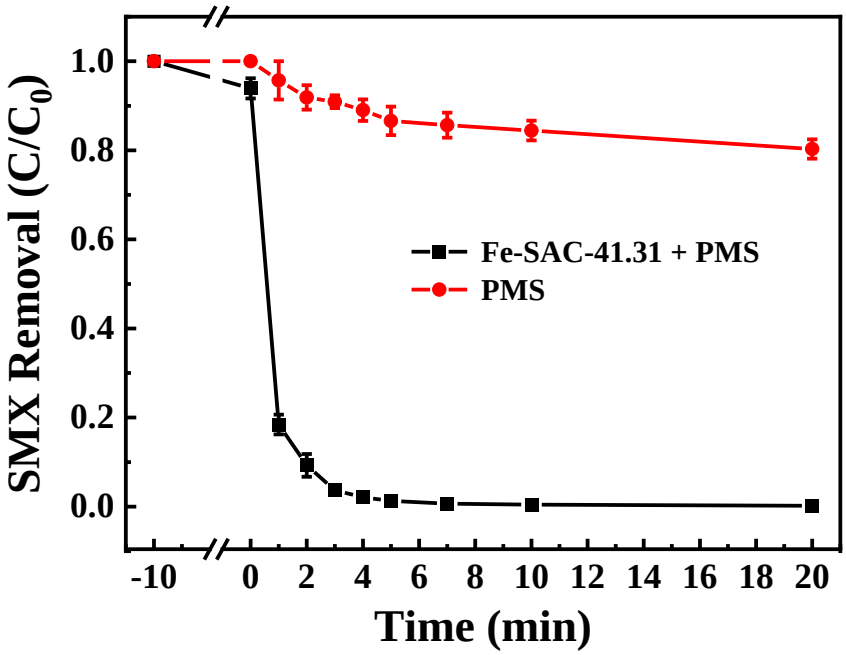

Supplementary Fig. 15 | Degradation effect of PMS on SMX.

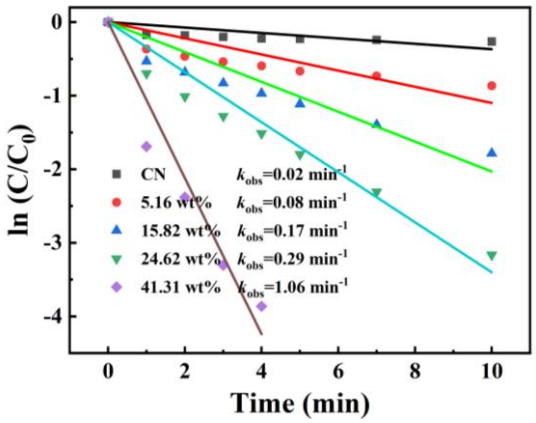

Supplementary Fig. 16 | The degradation kinetics of SMX in Fe-SAC-x/PMS system.

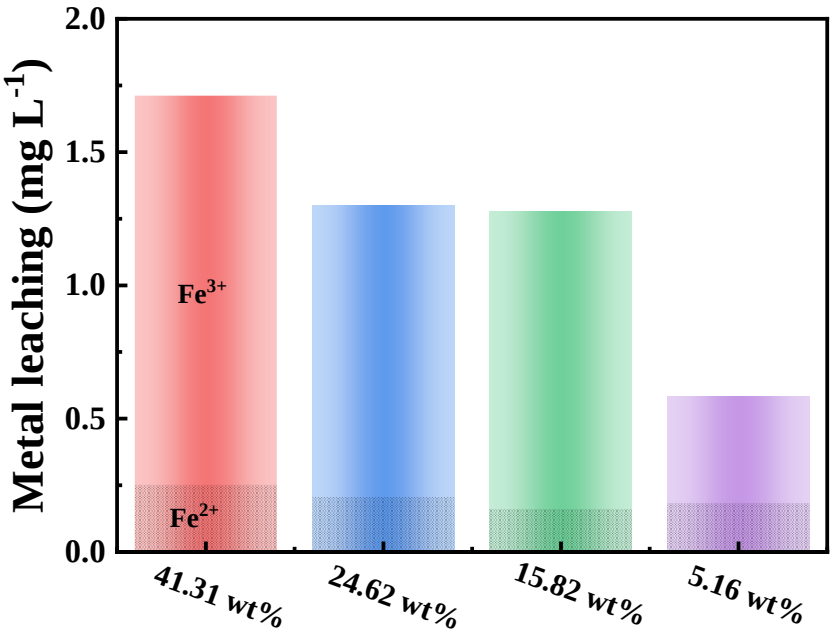

Supplementary Fig. 17 | Iron dissolution of Fe-SAC-x during degradation.

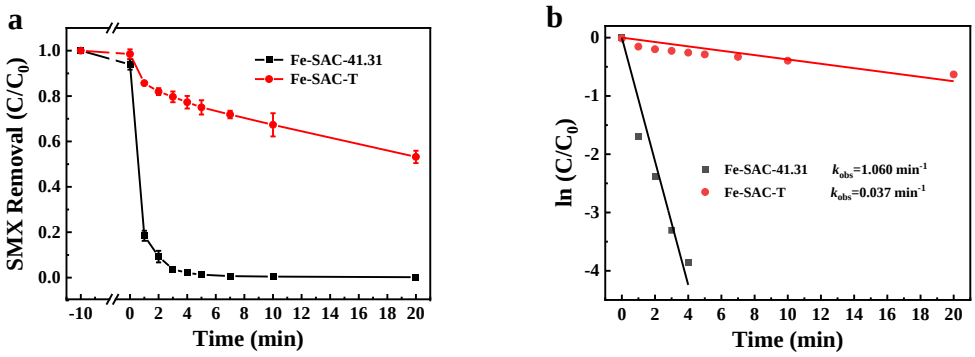

Supplementary Fig. 18 | a, SMX degradation performance. **b,** SMX degradation kinetics in the Fe-SAC-41.31/PMS and Fe-SAC-T/PMS system, respectively. Experimental conditions: $[SMX]_0$ = 10 mg L^{-1}, $[PMS]_0$ = 2 mM, pH = 7, catalyst: 0.1g L^{-1}.

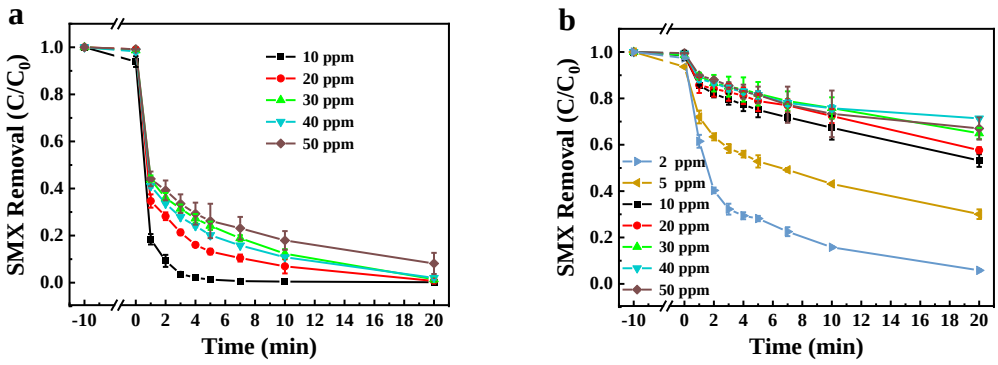

Supplementary Fig. 19 | Degradation performance of SMX at different initial concentrations in the **a,** Fe-SAC-41.31/PMS system **b,** Fe-SAC-T/PMS system, respectively. Experimental conditions: $[PMS]_0$ = 2 mM, pH = 7, catalyst: 0.1g L^{-1}.

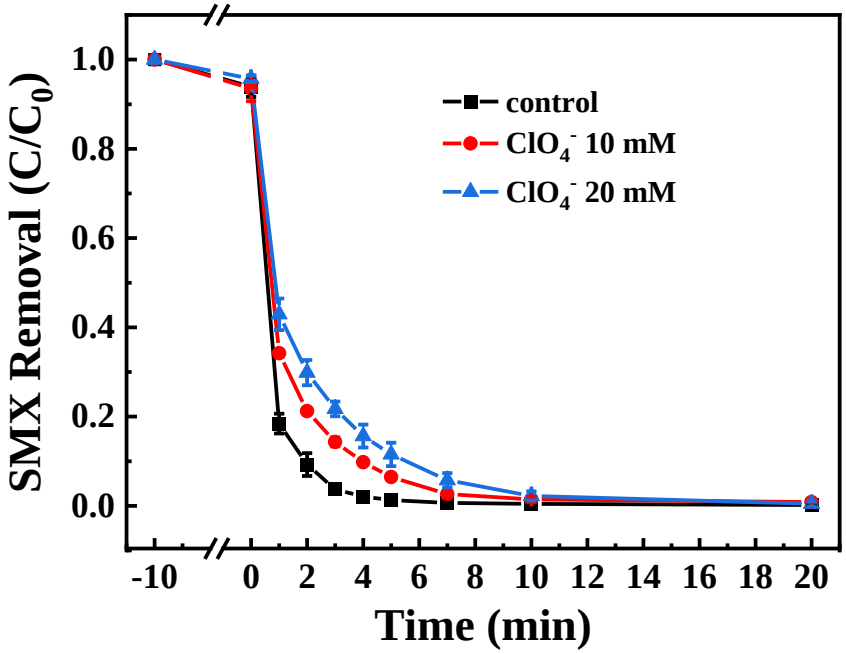

Supplementary Fig. 20 | Effect of ionic strength on SMX removal in Fe-SAC-41.31/PMS system.

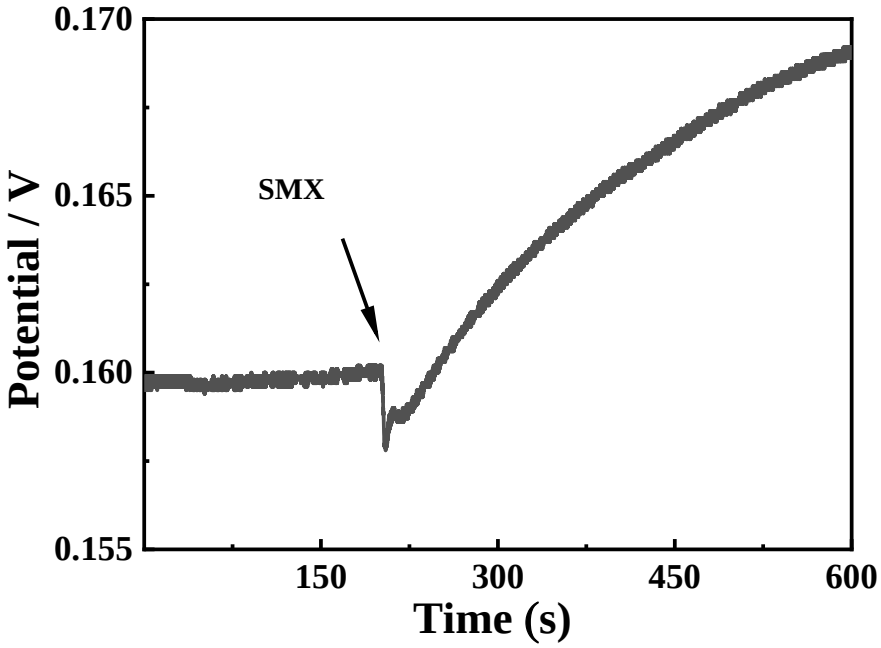

Supplementary Fig. 21 | Open-circuit potential change of Fe-SAC-41.31 with the addition of SMX.

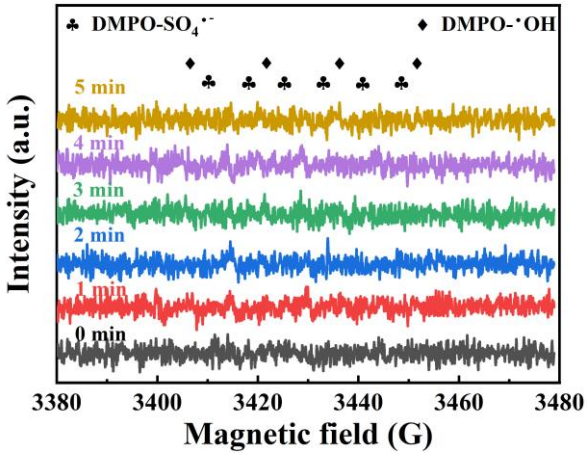

Supplementary Fig. 22 | EPR spectra of $^{\bullet}OH$ or $SO_4^{\bullet-}$ in the Fe-SAC-41.31/PMS system.

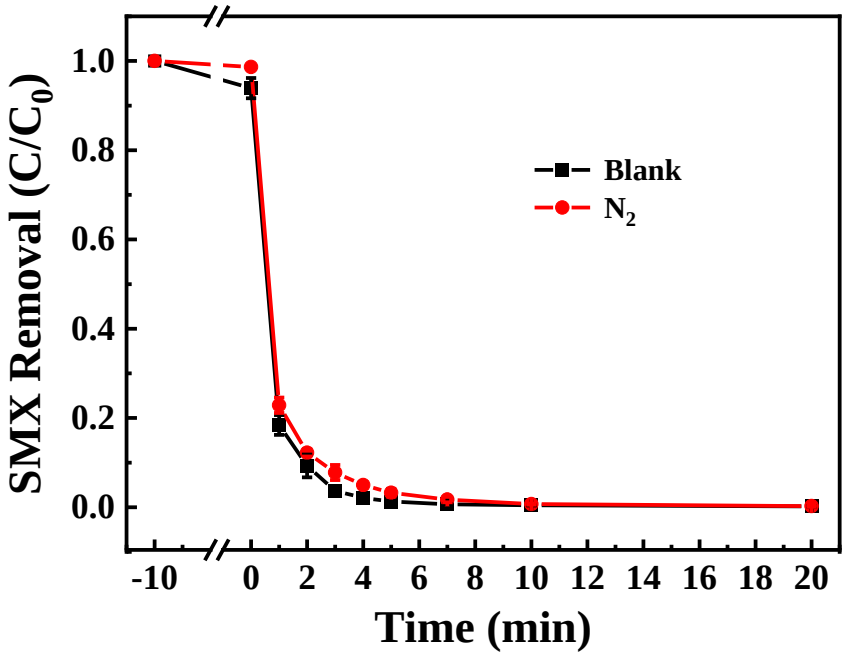

Supplementary Fig. 23 | Degradation performance of SMX with continuous injection of N_2 into the Fe-SAC-41.31/PMS system at a rate of 40 mL min^{-1}.

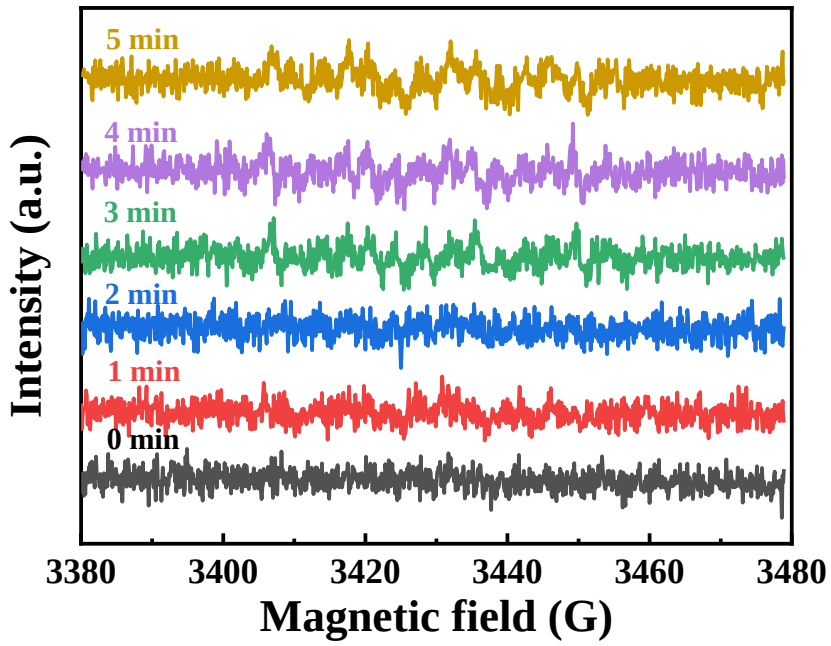

Supplementary Fig. 24 | EPR spectra of $O_2^{\bullet-}$ in the Fe-SAC-41.31/PMS system.

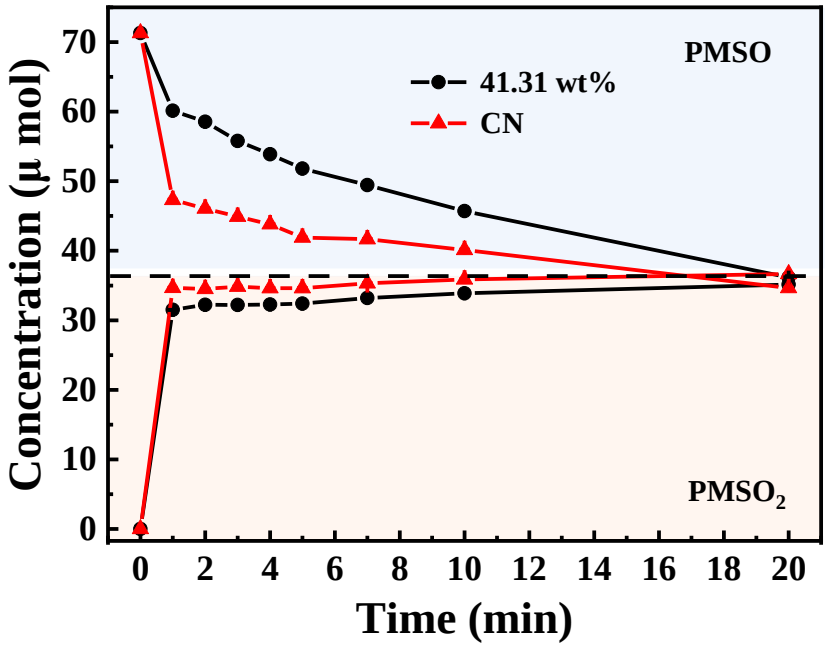

Supplementary Fig. 25 | Concentration changes of PMSO and $PMSO_2$ over reaction time. Reaction conditions: $[PMSO]_0$ = 10 mg L^{-1}, [PMS] = 2.0 mM.

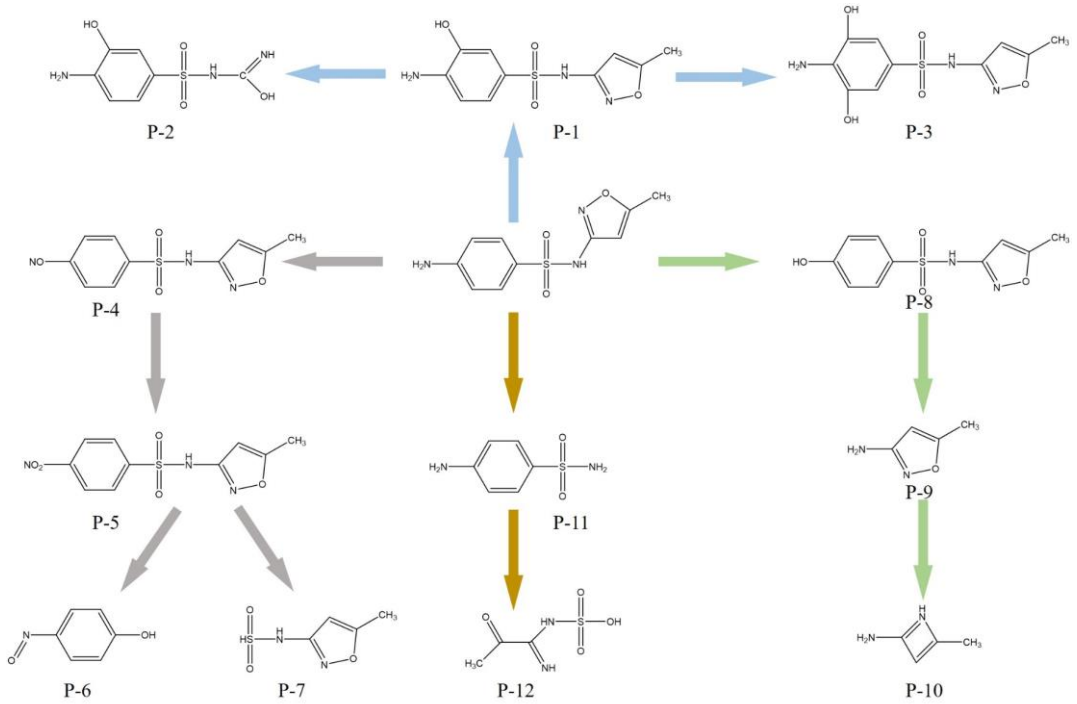

Supplementary Fig. 26 | SMX degradation pathways in the Fe-SAC-41.31/PMS system.

Supplementary Fig. 27 | Two possible oxygen adsorption configurations of Fe-C2N2 for PMS.

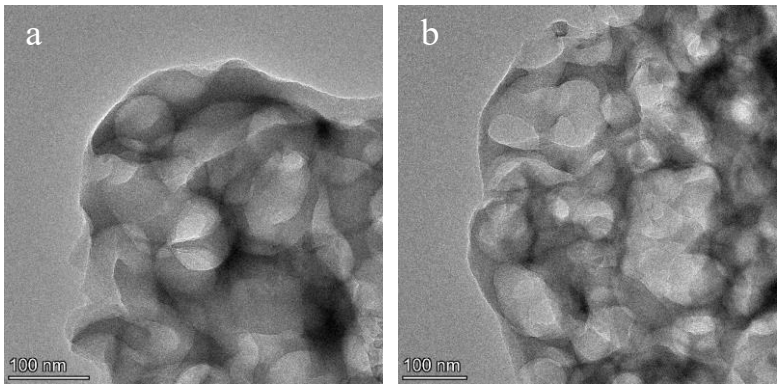

Supplementary Fig. 28 | a, b, TEM image of Fe-SAC-41.31 before and after the catalytic reaction.

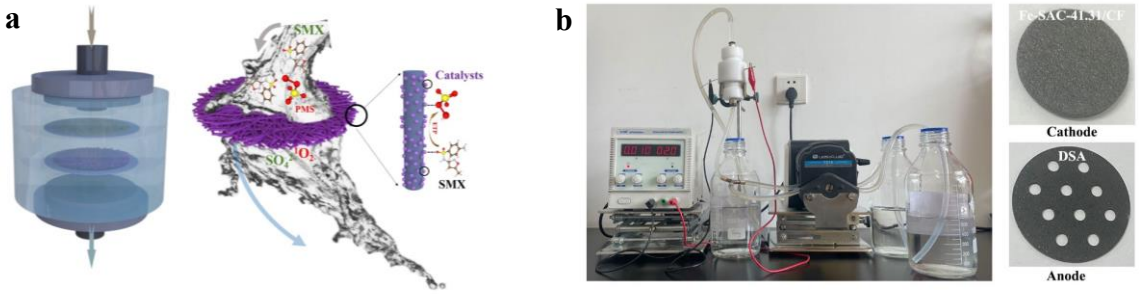

Supplementary Fig. 29 | a, Design principle of continuous flow device; **b,** Physical diagram of continuous flow device.

3. Supplementary Tables 1-32

Supplementary Table 1 | Fe content in varying samples.

Sample	Fe contents (wt%)
CN	0
Fe-SAC-T	1.61
Fe-SAC-5.16	5.16
Fe-SAC-15.82	15.82
Fe-SAC-24.62	24.62
Fe-SAC-41.31	41.31
Mn-SAC	35.13
Ag-SAC	27.04
La-SAC	22.62

Supplementary Table 2 | BET surface area, pore diameter and mesoporous pore volume of as-prepared catalysts.

Sample	BET surface (m^2/g)	Pore diameter (nm)	Mesoporous pore volume (cm^3/g)
NC	100.05	21.89	0.464
Fe-SAC 5.16 wt%	84.06	27.29	0.344
Fe-SAC 15.82 wt%	57.55	25.36	0.321
Fe-SAC 24.62 wt%	55.44	20.91	0.181
Fe-SAC 41.31 wt%	46.10	24.06	0.176

Supplementary Table 3 | EXAFS fitting parameters for various Fe-SAC-x samples.

Sample	Shell	N^a	$R(Å)^b$	$\sigma^2(Å^2)^c$	$\Delta E_0(eV)^d$	R factor
FePC	Fe-N	4	1.96	0.0068	1.9	0.0124
Fe-SAC-5.16	Fe-N	3.7	2.09	0.0132	4.91	0.0226
Fe-SAC-15.82	Fe-N	4.4	2.04	0.0171	3.4	0.0188
Fe-SAC-24.62	Fe-N	4.2	2.04	0.0195	5.15	0.0199
Fe-SAC-41.31	Fe-N	4.1	2.04	0.0196	4.44	0.0151

N^a: coordination numbers; $R(Å)^b$: bond distance; $\sigma^2(Å^2)^c$: Debye-Waller factors; $\Delta E_0(eV)^d$: the inner potential correction. R factor: goodness of fit. S_0^2 was set to 0.848, according to the experimental EXAFS fit of Fe foil by fixing CN as the known crystallographic value.

Supplementary Table 4 | Element contents and Fe density derived from XPS results.

Sample	Contents (at %)			
	C	N	$O_{(total)}$	Fe
NC	39.21	58.06	2.72	0
Fe-SAC 5.16 wt%	40.54	53.29	4.57	1.6
Fe-SAC 15.82 wt%	39.7	44.99	10.91	4.4
Fe-SAC 24.62 wt%	44.83	31.4	19.22	4.55
Fe-SAC 41.31 wt%	38.67	39.18	16.72	5.44

Supplementary Table 5 | Catalytic oxidation performances of various catalysts for pollutants.

Catalyst (g L^{-1})	Pollutant (mg L^{-1})	ROS	k value min^{-1}	Reference
High density Fe-SAC (0.1)	SMX (10)	ETP and $^1O_2$	**1.06**	This work
Cu-Fe^{vac}-LDH (0.1)	SMX (10)	Fe(IV)=O/Fe(V)=O	0.13	[4]
Fe@C-800 (0.4)	SMX (10)	$SO_4^{\bullet-}$, $^{\bullet}OH$, $O_2^{\bullet-}$ and $^1O_2$	0.074	[5]
Fe-NC-4 (0.15)	SMX (5.0)	$^1O_2$ and Fe(IV)=O	0.815	[6]
$CoSiO_x$ (0.4)	SMX (7.6)	$SO_4^{\bullet-}$ and $^{\bullet}OH$	0.47	[7]
Fe−Co−O−g-C_3N_4 (0.2)	SMX (10)	$SO_4^{\bullet-}$ and $^1O_2$	0.085	[8]
High density Fe-SAC (0.1)	BPA (10)	ETP and $^1O_2$	**1.269**	This work
Co-NC_4 (0.15)	BPA (10)	$SO_4^{\bullet-}$, $^{\bullet}OH$ and $^1O_2$	0.69	[9]
Fe-SAC (0.2)	BPA (25)	$^1O_2$	0.104	[10]
Co -SAC (0.2)	BPA (25)	$^1O_2$	0.083	[10]
CuO_4N_1 (0.6)	BPA (20)	$SO_4^{\bullet-}$, $^{\bullet}OH$, ETP and $^1O_2$	~0.01	[11]
CuCoNi−NF	BPA (10)	ETP	0.124	[12]
High density Fe-SAC (0.1)	BP (10)	ETP and $^1O_2$	**1.084**	This work
ZnFe-LDH (0.2)	BP (10)	Fe(IV)=O	0.1	[13]
CuO_4N_1 (0.6)	BP (20)	$SO_4^{\bullet-}$, $^{\bullet}OH$, ETP and $^1O_2$	~0.025	[11]
FeN_x−C (0.2)	BP (10)	$SO_4^{\bullet-}$, $^1O_2$ and Fe(V)=O	0.013	[14]
High density Fe-SAC (0.1)	TC (20)	ETP and $^1O_2$	**1.575**	This work
xCCH/CN−Vn (0.04)	TC (20)	Co(IV) =O and $^1O_2$	0.25	[15]
Co-N-GC (0.06)	TC (50)	$SO_4^{\bullet-}$, $^{\bullet}OH$ and $^1O_2$	0.04	[16]
Cu-In_2O_3/O_v (0.5)	TC (20)	$SO_4^{\bullet-}$ and $^{\bullet}OH$	0.26	[17]
CuO_4N_1 (0.6)	TC (20)	$SO_4^{\bullet-}$, $^{\bullet}OH$, ETP and $^1O_2$	~0.3	[11]
High density Fe-SAC (0.1)	RhB (10)	ETP and $^1O_2$	**0.987**	This work
g-C_3N_4 @NPC (0.08)	RhB (10)	$SO_4^{\bullet-}$, $^{\bullet}OH$, $O_2^{\bullet-}$ and $^1O_2$	0.152	[18]
High density Fe-SAC (0.1)	MO (10)	ETP and $^1O_2$	**6.11**	This work
biochar	MO (10)	$SO_4^{\bullet-}$ and $^{\bullet}OH$	0.127	[19]

Supplementary Table 6 | Intermediates detected by LC-MS in the Fe-SAC-41.31/PMS system.

Product	m/z	Molecular formula	Proposed structure
SMX	254.05938	$C_{10}H_{11}N_3O_3S$	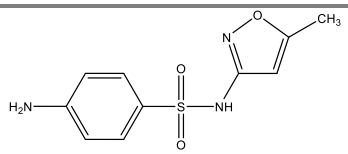
P1	270.05430	$C_{10}H_{11}N_3O_4S$	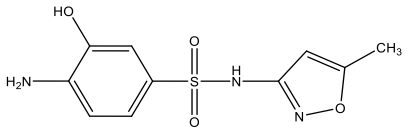
P2	232.03865	$C_7H_9O_4N_3S$	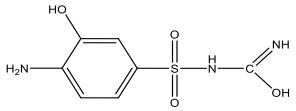
P3	286.04921	$C_{10}H_{11}O_5N_3S$	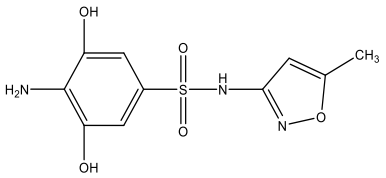
P4	268.03865	$C_{10}H_9O_4N_3S$	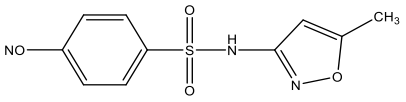
P5	284.03356	$C_{10}H_9O_5N_3S$	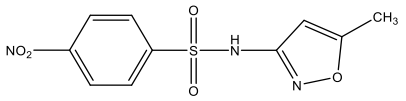
P6	124.03930	$C_6H_5NO_2$	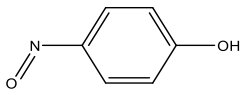
P7	163.01718	$C_4H_6O_3N_2S$	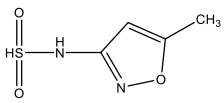
P8	255.04340	$C_{10}H_{10}O_4N_2S$	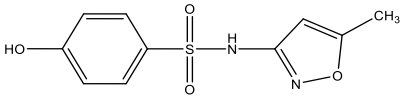

P9	99.05528	$C_4H_6ON_2$	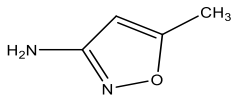
P10	83.06037	$C_4H_6N_2$	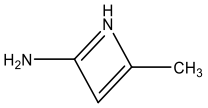
P11	173.03792	$C_6H_8N_2O_2S$	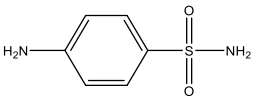
P12	167.01210	$C_3H_6N_2O_4S$	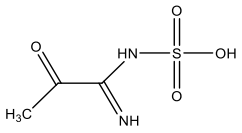

Supplementary Table 7 | The adsorption energy and bond length of Fe-O, O-O and O-H in the possible two adsorption configurations.

Adsorption site	$\triangle E_{ads}$ (eV)	Fe-O (Å)	O-O (Å)	O-H (Å)
O1	-2.54	1.971	1.463	0.986
O2	-2.53	1.961	1.487	0.998

Supplementary Table 8 | The Gibbs free-energy (△E) for every step in the two possible pathways of Fe-SAC-41.31 system.

Path I	$\triangle E_{ads}$ (eV) (HSO_5^-)	$\triangle E_{dis}$ (eV) ($^*SO_4^-$+*OH)	$\triangle E_{des}$ (eV) ($^*SO_4^-$)	$\triangle E_{dis}$ (eV) (*O+*H)	$\triangle E_{des}$ (eV) (*O)	Total (eV)
	-1.53	3.91	2.83	0.53	1.34	7.08
Path II	$\triangle E_{ads}$ (eV) (HSO_5^-)	$\triangle E_{dis}$ (eV) ($^*SO_5^-$+*H)	$\triangle E_{des}$ (eV) (*H)	$\triangle E_{des}$ (eV) ($^*SO_5^-$)	/	Total (eV)
	-1.53	3.54	2.86	1.03		5.90

Supplementary Table 9 | The Gibbs free-energy (△E) for every step in the possible pathway of different catalysts.

Sample (wt%)	$\triangle E_{ads}$ (eV) (HSO_5^-)	$\triangle E_{dis}$ (eV) ($^*SO_5^-$+$^*H$)	$\triangle E_{des}$ (eV) ($^*H$)	$\triangle E_{des}$ (eV) ($^*SO_5^-$)	Total (eV)
5.16	-2.04	5.52	1.11	2.49	7.08
15.82	-1.99	5.49	1.17	2.17	6.84
24.62	-1.38	4.64	1.19	0.06	4.51
41.31	-1.53	3.54	2.86	1.03	5.90

Supplementary Table 10 | The quality parameters of the wastewater.

	Tap water	Medical wastewater	Mati Lake
pH	7.5	7.53	8.02
Conductivity (μS cm^{-1})	330	21.70	1193
COD (mg L^{-1})	3.0	145.0	32.6
TOC (mg L^{-1})	1.56	102.5	31.7
Cl^- (mg L^{-1})	2.11	502.1	420.6
HCO_3^- (mg L^{-1})	108	48.3	83.1
NO_3^- (mg L^{-1})	0.3	18.3	50.8

Supplementary Table 11 | The quality parameters of the coal reverse osmosis water.

	Detection value
pH	9.41
Conductivity (μS cm^{-1})	18400
TOC (mg L^{-1})	69.725
TDS (mg L^{-1})	9200
TN (mg L^{-1})	194.75
Suspension (mg L^{-1})	0.045
Saturation	D=30, buff
UV254 (cm^{-1})	0.675
Cl^- (mg L^{-1})	4108.65
SO_4^{2-} (mg L^{-1})	604.223
NO_3^- (mg L^{-1})	789.543
NO_2^- (mg L^{-1})	2.828
NH_4^+	8.31

Supplementary Table 12 | 3DEEM response and their associated characteristics.

Region	I	II	III	IV
Excitation Wavelength	200-250 nm	200-250 nm	250-300 nm	250-500 nm
Emission Wavelength	280-380 nm	380-600 nm	280-380 nm	380-500 nm
Characteristics	Fluorophores associated with aromatic-like molecules (Tyrosine)	Fluorophores associated with fulvic acid-like molecules	Fluorophores associated with SMP-like molecules (Tryptophane)	Fluorophores associated with humic acid-like molecules

Supplementary Table 13 | The HPLC analysis conditions for different substrates.

Substrates	Flow (ml/min)	λ (nm)	CH_3OH (%)	Acetonitrile (%)	H_2O (%)
BPA	0.5	280	70	/	30
TC	0.5	275	/	18	82(0.1% H_3PO_4)
SMX	0.5	265	35	/	65
SMT	0.5	280	35	/	65

4. Supplementary References

(1) Hohenberg, P.; Kohn, W. Inhomogeneous Electron Gas. *Physical Review* **1964**, *136* (3B), B864-B871.

(2) Kohn, W.; Sham, L. J. Self-Consistent Equations Including Exchange and Correlation Effects. *Physical Review* **1965**, *140* (4A), A1133-A1138.

(3) Perdew, J. P.; Burke, K.; Ernzerhof, M. Generalized gradient approximation made simple. *Physical Review Letters* **1996**, *77* (18), 3865.

(4) Zhou, X.; Yin, R.; Kang, J.; Li, Z.; Pan, Y.; Bai, J.; Li, A. J.; Qiu, R. Atomic cation-vacancy modulated peroxymonosulfate nonradical oxidation of sulfamethoxazole via high-valent iron-oxo species. *Appl. Catal. B Environ.* **2023**, *330*, 122640.

(5) Pu, M.; Wan, J.; Zhang, F.; Brusseau, M. L.; Ye, D.; Niu, J. Insight into degradation mechanism of sulfamethoxazole by metal-organic framework derived novel magnetic Fe@C composite activated persulfate. *J. Hazard. Mater.* **2021**, *414*, 125598.

(6) Wang, J.; Li, B.; Li, Y.; Fan, X. B.; Zhang, F. B.; Zhang, G. L.; Peng, W. C. Facile synthesis of atomic Fe-N-C materials and dual roles investigation of Fe-N-4 sites in fenton-like reactions. *Adv. Sci.* **2021**, *8* (22), 2101824.

(7) Liu, X.; Chen, C.; Chen, P.; Wang, L. Ultrafast degradation of SMX and TC by $CoSiO_x$ activated peroxymonosulfate: efficiency and mechanism. *RSC Adv.* **2023**, *13* (5), 3103-3111, 10.1039/D2RA06865F.

(8) Wang, S. Z.; Liu, Y.; Wang, J. L. Peroxymonosulfate activation by Fe-Co-O-Co doped graphite carbon nitride for degradation of sulfamethoxazole. *Environ. Sci.*

Technol. **2020**, *54* (16), 10361-10369.

(9) Liang, X.; Wang, D.; Zhao, Z.; Li, T.; Gao, Y.; Hu, C. Coordination number dependent catalytic activity of single-atom cobalt catalysts for fenton-like reaction. *Adv. Funct. Mater.* **2022**, *32* (38), 2203001.

(10) Gao, Y.; Wu, T.; Yang, C.; Ma, C.; Zhao, Z.; Wu, Z.; Cao, S.; Geng, W.; Wang, Y.; Yao, Y.; et al. Activity trends and mechanisms in peroxymonosulfate-assisted catalytic production of singlet oxygen over atomic Metal-N-C catalysts. *Angew. Chem. Int. Ed.* **2021**, *60* (41), 22513-22521.

(11) Mi, X.; Zhong, H.; Zhang, H.; Xu, S.; Li, Y.; Wang, H.; Zhan, S.; Crittenden, J. C. Facilitating redox cycles of copper species by pollutants in peroxymonosulfate activation. *Environ. Sci. Technol.* **2022**, *56* (4), 2637-2646.

(12) Wang, M. M.; Liu, L. J.; Wen, J. T.; Ding, Y.; Xi, J. R.; Li, J. C.; Lu, F. Z.; Wang, W. K.; Xu, J. Multimetallic CuCoNi oxide nanowires in situ grown on a nickel foam substrate catalyze persulfate activation via mediating electron transfer. *Environ. Sci. Technol.* **2022**, *56* (17), 12613-12624.

(13) Bao, Y.; Lian, C.; Huang, K.; Yu, H.; Liu, W.; Zhang, J.; Xing, M. Generating High-valent Iron-oxo $\equiv Fe^{IV}=O$ Complexes in Neutral Microenvironments through Peroxymonosulfate Activation by Zn−Fe Layered Double Hydroxides. *Angew. Chem. Int. Ed.* **2022**, *61* (42), e202209542.

(14) Zhang, B.; Li, X.; Akiyama, K.; Bingham, P. A.; Kubuki, S. Elucidating the mechanistic origin of a spin state-dependent FeN_x–C catalyst toward organic contaminant oxidation via peroxymonosulfate activation. *Environ. Sci. Technol.* **2022**,

56 (2), 1321-1330.

(15) Jiang, J.; Zhao, Z.; Gao, J.; Li, T.; Li, M.; Zhou, D.; Dong, S. Nitrogen vacancy-modulated peroxymonosulfate nonradical activation for organic contaminant removal via high-valent cobalt-oxo species. *Environ. Sci. Technol.* **2022**, *56* (9), 5611-5619.

(16) Ma, S.; Yang, D.; Guan, Y.; Yang, Y.; Zhu, Y.; Zhang, Y.; Wu, J.; Sheng, L.; Liu, L.; Yao, T. Maximally exploiting active sites on Yolk@shell nanoreactor: Nearly 100% PMS activation efficiency and outstanding performance over full pH range in Fenton-like reaction. *Appl. Catal. B Environ.* **2022**, *316*, 121594.

(17) Zhao, Z.; Wang, P.; Song, C.; Zhang, T.; Zhan, S.; Li, Y. Enhanced interfacial electron transfer by asymmetric Cu-O_v-In sites on In_2O_3 for efficient peroxymonosulfate activation. *Angew. Chem. Int. Ed.* **2023**, *62* (11), e202216403.

(18) Kong, L.-H.; Wu, Y.; Shen, R.-F.; Zhang, W.-J.; Dong, Z.-Y.; Ge, W.-T.; Guo, X.-J.; Yan, X.; Chen, Y.; Lang, W.-Z. Combination of N-doped porous carbon and g-C_3N_4 for effective removal of organic pollutants via activated peroxymonosulfate. *J. Environ. Chem. Eng.* **2022**, *10* (3), 107808.

(19) Mian, M. M.; Liu, G. Activation of peroxymonosulfate by chemically modified sludge biochar for the removal of organic pollutants: Understanding the role of active sites and mechanism. *Chem. Eng. J.* **2020**, *392*, 123681.